

Geometrical Computations Explain Projection Patterns of Long-Range Horizontal Connections in Visual Cortex

Ohad Ben-Shahar

ben-shahar@cs.yale.edu

Steven Zucker

zucker-steven@cs.yale.edu

*Department of Computer Science and the Interdepartmental Neuroscience Program,
Yale University, New Haven, CT 06520, U.S.A.*

Neurons in primary visual cortex respond selectively to oriented stimuli such as edges and lines. The long-range horizontal connections between them are thought to facilitate contour integration. While many physiological and psychophysical findings suggest that collinear or association field models of good continuation dictate particular projection patterns of horizontal connections to guide this integration process, significant evidence of interactions inconsistent with these hypotheses is accumulating. We first show that natural random variations around the collinear and association field models cannot account for these inconsistencies, a fact that motivates the search for more principled explanations. We then develop a model of long-range projection fields that formalizes good continuation based on differential geometry. The analysis implicates curvature(s) in a fundamental way, and the resulting model explains both consistent data and apparent outliers. It quantitatively predicts the (typically ignored) spread in projection distribution, its nonmonotonic variance, and the differences found among individual neurons. Surprisingly, and for the first time, this model also indicates that texture (and shading) continuation can serve as alternative and complementary functional explanations to contour integration. Because current anatomical data support both (curve and texture) integration models equally and because both are important computationally, new testable predictions are derived to allow their differentiation and identification.

1 Introduction ---

The receptive fields (RFs) of neurons in visual cortex characterize their response to patterns of light in the visual field. In primary visual cortex, this response is often selective for stimulus orientation in a small region (Hubel & Wiesel, 1977). The clustered long-range horizontal connections between such cells (Rockland & Lund, 1982) link those with nonoverlapping RFs and

are thought to facilitate contour integration (Field, Hayes, & Hess, 1993). However, there is no direct physiological evidence that these connections *only* support curve integration, while there also remains much ambiguity about the precise connections required to support the integration of curves. Our goal in this article is to address both of these concerns.

1.1 Biological Data and Integration Models. The argument that associates long-range horizontal connections with curve integration begins with the realization that the finite spatial extent of RFs and their broad orientation tuning lead to significant uncertainties in the position and the local orientation measured from visual stimuli. This causes a further uncertainty in determining which of the many nearby RFs signal the next section of a curve (see Figure 1a).

All of these uncertainties underlying curve integration can be reduced by interactions between neurons whose RFs are close in retinotopic coordinates. Starting with Mitchison and Crick (1982) and their hypothesis about interactions between iso-oriented RFs, physiological and anatomical findings have been accumulating to suggest a roughly collinear interaction. The main evidence supporting this conclusion is based on the distribution of angular differences between preferred orientations of connected cells. These distributions are computed by taking the orientation difference between a target cell and every other cell it is connected to with a long-range horizontal connection. Indeed, as is exemplified in Figure 1b, these distributions have been shown to be unimodal on average, with maximal interaction between iso-oriented RFs (Ts'o, Gilbert, & Wiesel, 1986; Gilbert & Wiesel, 1989; Weliky, Kandler, Fitzpatrick, Katz, 1995; Schmidt, Goebel, Löwel, & Singer, 1997; Buzás, Eysel, Kisvárdy, 1998; Bosking, Zhang, Schofield, & Fitzpatrick, 1997; Malach, Amir, Harel, & Grinvald, 1993; Sincich & Blasdel, 2001; Schmidt & Löwel, 2002). Furthermore, direct anatomical studies reveal long-range interactions between coaxial cells (Bosking et al., 1997; Schmidt et al., 1997) and indirect psychophysical experiments report a general association field (Field et al., 1993; Kapadia, Ito, Gilbert, & Westheimer, 1995; Kapadia, Westheimer, & Gilbert, 2000) which emphasizes straight or slowly varying continuations while allowing some support for more rapidly varying continuations as well (see Figure 2a).

With the accumulation of these data, however, are a growing number of observations that are difficult to reconcile with the intuition that neural spatial integration is based on collinearity or that it serves only curve integration. Facilitory interaction between cells of significant orientation difference (Kapadia et al., 1995) short-range coaxial inhibition (Polat & Sagi, 1993), iso-orientation side facilitation (Adini, Sagi, & Tsodyks, 1997), and strong correlations between iso-oriented, nonoverlapping, and parallel receptive fields (Ts'o et al., 1986) are functionally inconsistent. Evidence of cross-orientation (Matsubara, Cynader, Swindale, & Stryker, 1985; Kisvárdy, Tóth, Rausch, & Eysel, 1997) and nonaxial (Gilbert & Wiesel, 1989) connections, plus roughly

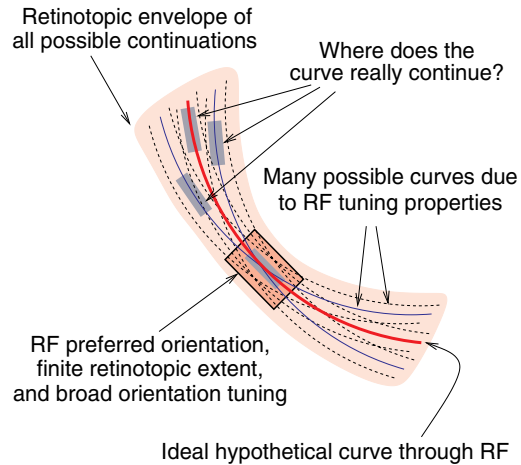
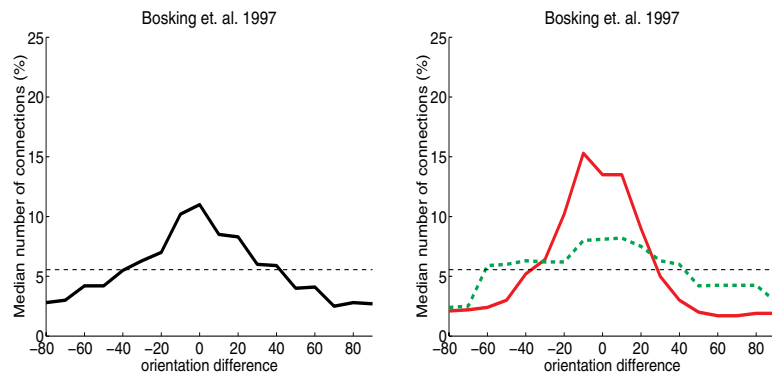
**a****b****c**

Figure 1: Visual integration and the distribution of long-range projections. (a) Broad tuning in orientation and position introduce uncertainty in curve integration even if a single curve model (thick red curve) is assumed through the RF. Determining which nearby RF the curve continues through can be facilitated by interaction between neurons with mutually aligned, retinotopically close RFs. (b) A fundamental measurable property of long-range connection is their distribution in the orientation domain, that is, the percentage of connections between interconnected neurons as a function of preferred orientation (angular) difference. This graph shows the median distribution of lateral connections (distance $> 500\mu\text{m}$) of seven cell clusters in primary visual cortex of tree shrew (redrawn from Bosking et al., 1997, their Fig. 6c). Qualitatively similar (through coarser) measurements are available on primates as well (Malach et al., 1993). (c) Connectivity distribution of individual cell clusters reveals significant variability and qualitative differences between them. Shown here are distributions from two injection sites from Bosking et al. (1997).

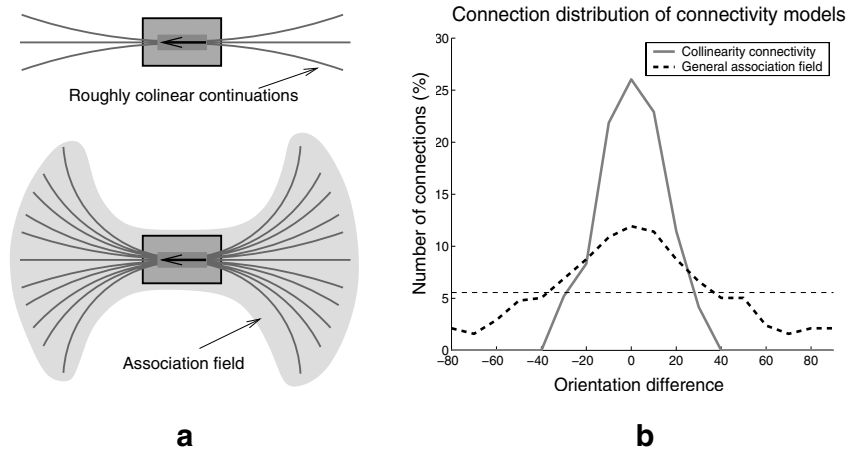


Figure 2: Collinear facilitation, association fields, and their predicted distribution of connections. (a) Informally, two visual integration or continuation models are typically considered in the physiological and psychophysical literatures. Collinearity, the predominant model, predicts only few possible curve continuations (top). On the other hand, many possible continuations reveal an association field (bottom), similar to those observed psychophysically (Field et al., 1993). (b) The corresponding distribution derived from the collinearity and association field models. Observe that collinearity predicts a very narrow distribution, which is clearly at odds with the significant spread frequently measured anatomically or electrophysiologically (compare to Figure 1b). The association field leads to a wider spread, but like collinearity, it predicts a fixed distribution for all cells, a hypothesis refuted in recent studies (see the text). The collinearity distribution (solid) was calculated from the field depicted in Figure 8a, while the association field distribution (dashed) was calculated from the field in Figure 8e. The dashed horizontal line depicts the uniform distribution.

isotropic retinotopic extent (Malach et al., 1993; Sincich & Blasdel, 2001), suggest anatomical inconsistencies.

These inconsistencies prompt a closer examination of the interactions within visual cortex and their population statistics. As the evidence suggests, individual cells, or small collections of adjacent cells captured in tracer injections, may have qualitatively different connectivity distributions (Bosking et al., 1997): some are narrow and high while others are very wide, as is illustrated in Figure 1c. When averaged, the pooled distribution of long-range connections (e.g., those extending beyond 500 μm in Bosking et al., 1997) is (see Figure 3a):

- Unimodal.
- Peaks at zero orientation offset.

- Indicates a nonnegligible fraction of connections linking cells of significantly different orientation preferences (Malach et al., 1993; Kisvárdy, Kim, Eysel, & Bonhoeffer, 1994; Kisvárdy et al., 1997; Bosking et al., 1997).
- Crosses the uniform distribution at approximately ± 40 degrees.¹
- Has a *nonmonotonically* changing variance as the orientation difference increases (Malach et al., 1993; Bosking et al., 1997).

Neither collinearity nor association field models predict all of these features. While both models imply unimodal pooled distributions over orientation differences (see Figure 2b), they also suggest a fixed projection field and thus neither predicts any variance for the pooled distribution, let alone a nonmonotonic one. Furthermore, collinearity is clearly at odds with the significant spread in the distribution of connections over orientation differences, whether it is measured via extracellular injections (e.g., Bosking et al., 1997) or the more elaborate intracellular protocol (Buzás et al., 1998).

The data in Bosking et al. (1997) contain one injection site of possibly different connection distribution, which may substantially contribute to the nonmonotonic nature of the variance. Since the variance will become central to this article, we examined whether this statistical feature depends critically on this one, possibly outlier, measurement. We reanalyzed the data from Bosking et al. (1997) after removing the data from this injection site and calculating the statistical properties of the rest. We further examined the robustness of the nonmonotonicity by running two additional analyses: one in which we removed the sample points (one from each orientation bin) that contribute the most to the variance, and another in which we removed those sample points (again, one from each bin) that maximized local changes in the variance. In all these tests, including the last one, which flattens the variance the most, the trimodal nonmonotonicity, and the two local minima at ± 30 degrees, were preserved. All these findings suggest that the nonmonotonicity of the variance is a critical feature that deserves attention from both biologists and modelers.

1.2 Integration Models and Random Physiological Variations. It is tempting to explain the apparent anomalies and inconsistencies between the predicted and measured distributions of long-range horizontal connections as random physiological variations, for example, by asserting that anatomy only approximates the correct connections. We tested this explanation by applying different noise models to the collinearity and association field connectivity distributions from Figure 2, and checked whether the resul-

¹ This crossing point provides a reference for the bias of projection patterns toward particular orientations; considering the offsets where the connection distribution crosses the uniform line quantifies this bias in a way independent of scale or quantization level.

tant pooled distributions possess the properties listed above. The results of the most natural noise model are illustrated in Figure 3b. Under this model, each long-range horizontal connection, ideally designated to connect cells of orientation difference $\Delta\theta$, is shifted to connect cells of orientation difference $\Delta\theta + \epsilon_\sigma$, where ϵ_σ is a wrapped gaussian (i.e., normally distributed and wrapped on \mathcal{S}^1) random variable with zero mean and variance σ (see the appendix for details). As the figure shows, it takes an overwhelming amount of noise (s.d. ≥ 35 degrees) to transform the collinear distribution to one that resembles the measured data in terms of spread and peak height, but the nonmonotonic behavior of the variance is never reproduced. (For space considerations, we omit the results of other connection-based noise models, or the noisy distributions based on the association field model, all of which were even less reminiscent of the measured physiological data.)

A second possible source for the inconsistencies between the predicted and measured distributions may be the extracellular injection protocol commonly in use by physiologists to trace long-range horizontal connections (e.g., Gilbert & Wiesel, 1989; Malach et al., 1993; Kisvárdy et al., 1994, 1997; Bosking et al., 1997; Schmidt et al., 1997; Sincich & Blasdel, 2001). Due to the site-selection procedure used, cells stained by these injections are likely to have similar orientation preferences (e.g., Bosking et al., 1997, p. 2113, or Schmidt et al., 1997, p. 1084). However, their orientation tuning may nevertheless be different, sometimes significantly (note such a cell in Bosking et al., 1997, Fig. 4B). Consequently, the distribution of presynaptic terminals (boutons) traced from the injection site may incorporate an artificial, random spread relative to the single orientation typically assumed at the injection site. Preliminary evidence from a recently developed single-cell protocol (Buzás et al., 1998) suggests that leakage in the injection site cannot bridge the gap between the predicted collinear distribution and those measured anatomically. However, we also examined this possibility computationally by modeling the leakage in the injection site as a wrapped gaussian random variable of predefined variance.² The base distributions (collinear or association field) of the computational cells selected by this process were then summed up and normalized, and the resultant (random) distribution was attributed to the original cell representing the injection site. Repeating this process many times yielded a collection of (different) distributions, for which we calculated an average and variance (see the appendix for details). The results are illustrated in Figure 3c. Similar to random variations at the level of individual connections, here too it takes an overwhelming amount of noise (s.d. ≥ 35 degrees) to transform the collinear distribution to one that resembles the measured data in terms of spread and peak height, but the nonmonotonic behavior of the variance is never reproduced.

² A wrapped gaussian model was particularly suitable here due to the injection site selection protocol typically used in the extracellular injection protocol; see the appendix.

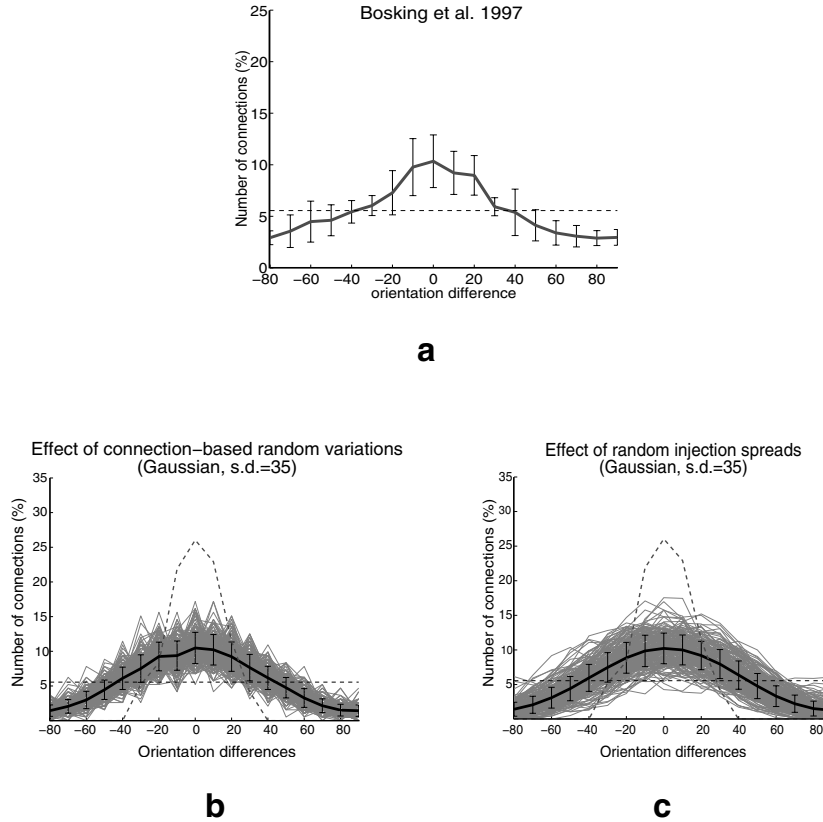


Figure 3: Results of a statistical perturbation of collinear connectivity distribution. (a) Mean connection distribution computed from the data in Bosking et al. (1997), shown here for reference. Error bars are ± 1 standard deviation. Note the unimodal distribution that peaks at approximately 11%, the wide spread, crossing of the uniform distribution (dashed horizontal line) around ± 40 degrees, and the nonmonotonic variance. Can all these features be replicated by applying noise to the base distribution induced by the standard collinearity model? (b) Result of simulating physiological deviation at the individual connection level. The dashed line is the base collinear distribution. The gray region is the superposition of individual applications of the noise model to the base distribution. The solid graph is the expected distribution, and error bars are ± 1 standard deviation. Permitting large enough developmental variations (shown here is the result of wrapped gaussian independent and identically distributed noise of s. d. = 35°) in the connections to model the first-order statistics significantly violates the underlying connectivity principle of good continuation but still cannot model the second-order statistics. (c) Results of simulating measurement errors due to leakage in the injection site. All parts are coded as in *b*. Again, permitting large enough injection spread to model the first-order statistics (shown here is the result of gaussian noise of s.d. = 35° and assuming 20 cells per injection site; (Bosking et al., 1997) cannot model the second-order statistics

The thinking around long-range horizontal connections has been dominated by their first-order statistics and its peak at zero orientation offset. However, the nonmonotonicity of the variance was first reported almost a decade ago (Fig. 3d in Malach et al., 1993) and we have further confirmed it from the more detailed measurements in Bosking et al. (1997) as was illustrated in Figure 3a. Since neither collinearity nor association field models can explain this aspect of the physiological data, even if much noise is allowed, it is necessary to consider whether this and the other subtle properties of the pooled data reflect genuine functional properties of long-range horizontal connections. We therefore developed a geometric model of projection patterns and examined quantitatively both pooled connection statistics and connectivity patterns of individual cells generated by it. Since many findings suggest that long-range horizontal connections are primarily excitatory, especially those extending beyond one hypercolumn (Ts'o et al., 1986; Gilbert & Wiesel, 1989; Kapadia et al., 1995; Kisvárdy et al., 1997; Buzás et al., 1998; Sincich & Blasdel, 2001), our model concentrates on this class of connections.

2 From Differential Geometry to Integration Models ---

Curve integration, the hypothesized functional role ascribed to long-range horizontal connections, is naturally based in differential geometry. The tangent, or the local linear approximation to a curve, abstracts orientation preference, and the collection of all possible tangents at each (retinotopic) position can be identified with the orientation hypercolumn (Hubel & Wiesel, 1977). Formally, since position takes values in the plane \mathbb{R}^2 (think of image coordinates x, y) and orientation in the circle S^1 (think of an angle θ varying between 0 and 2π), the primary visual cortex can be abstracted as the product space $\mathbb{R}^2 \times S^1$ (see Figure 4). Points in this space represent both position and orientation to abstract visual edges of given orientation at a particular spatial (i.e., retinotopic) position. It is in this space that our modeling takes place.

Since any single tangent is the limit of any smooth curve passing through a given (retinotopic) point in a given direction, the question of curve integration becomes one of determining how two tangents at nearby positions are related. (Collinearity, for example, asserts that the tangent orientation hardly changes for small displacements along the curve.) In general terms, the angular difference between RFs captures only one part of the relationship between nearby tangents; their relative spatial offset also must be considered. Thus, in the mathematical abstraction, relationships between tangents correspond to relationships between points in $\mathbb{R}^2 \times S^1$. Physiologically, these relationships are carried by the long-range horizontal connections, with variation in retinotopic position corresponding to \mathbb{R}^2 , and variation along orientation hypercolumns corresponding to S^1 (see Figure 5). Determining them amounts, in mathematical terms, to determining what is called a con-

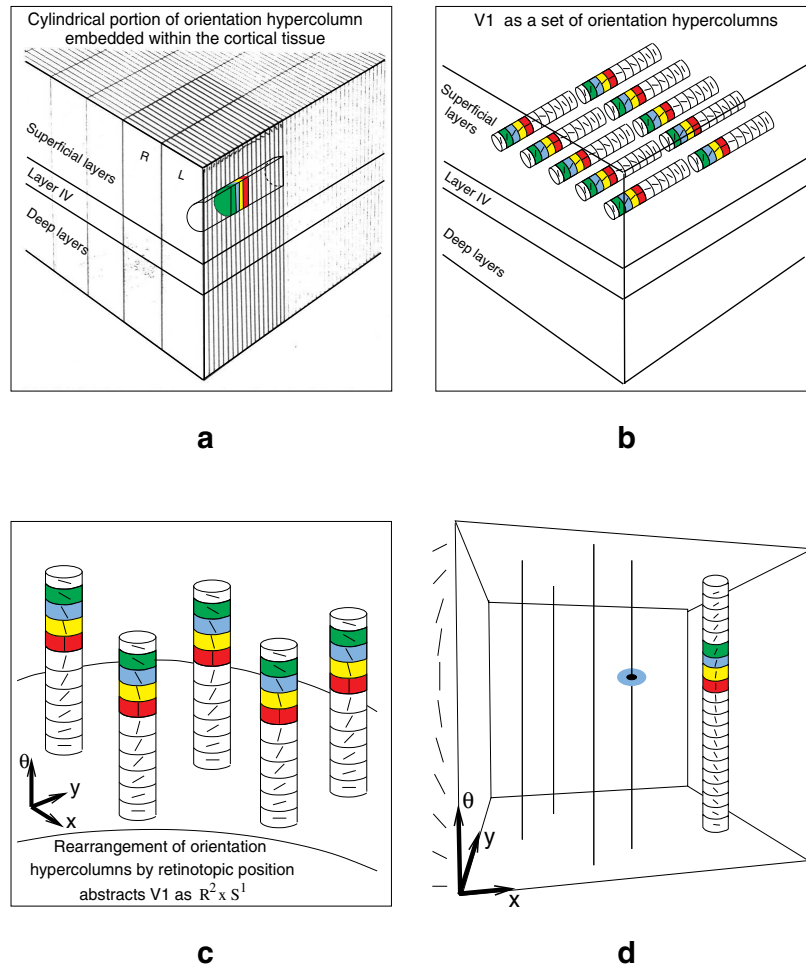
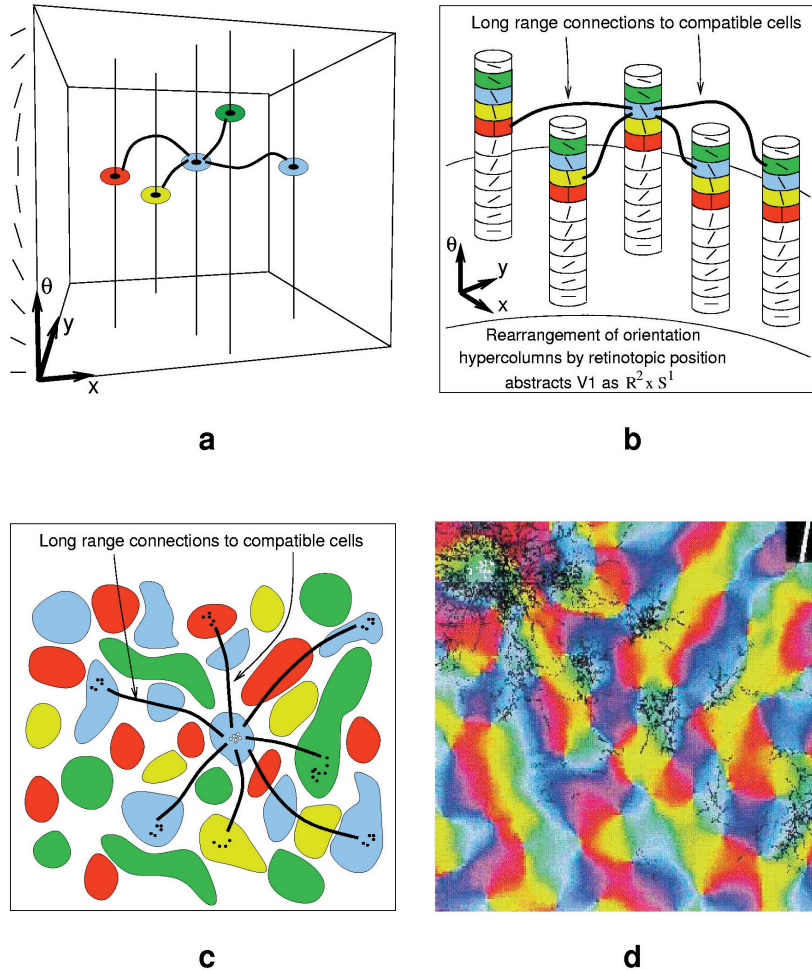


Figure 4: Abstracting the primary visual cortex as $\mathbb{R}^2 \times \mathcal{S}^1$, or position \times orientation space. (a) The “ice cube” cartoon of visual cortex (Hubel & Wiesel, 1977) (cytochrome-oxidase blobs and distortions due to cortical magnification factor are not shown). A tangential penetration in the superficial layers reveals an orientation hypercolumn of cells whose RFs have similar spatial (retinotopic) coordinates. With cells of similar orientation tuning grouped by color, the hypercolumn is cartooned as a horizontal cylinder. (b) With ocular dominance columns omitted, the superficial layers of the primary visual cortex can be viewed as a collection of (horizontally arranged) orientation hypercolumns. (c) Drawing the cylinders vertically emphasizes that RFs of cells within a column overlap in retinotopic coordinates (x, y) and makes explicit this aspect of their organization. (d) Since different hypercolumns correspond to different retinotopic positions, the set of all hypercolumns abstracts the visible subspace of $\mathbb{R}^2 \times \mathcal{S}^1$, with each column corresponding to a different vertical fiber in that space. The θ -axis in this space corresponds to a tangential penetration with V1 hypercolumns (colors within the column represent different orientation tunings), and the XY plane corresponds to retinotopic coordinates.



nection structure. As we discuss in the rest of this article, the relationship between these two types of connections, the mathematical and the physiological, is more than linguistic.

2.1 The Geometry of Orientation in the Retinal Plane. Orientation in the 2D (retinal) plane is best represented as a unit length tangent vector $\hat{E}(\vec{q})$ attached to point of interest $\vec{q} = (x, y) \in \mathbb{R}^2$. Having such a tangent vector attached to every point of an object of interest (e.g., a smooth curve or oriented texture) results in a unit length vector field (O'Neill, 1966). Assuming good continuation (Wertheimer, 1955), a small translation \vec{V} from the point \vec{q} results in a small change (i.e., rotation) in the vector $\hat{E}(\vec{q})$. To apply

techniques from differential geometry, a suitable coordinate frame $\{\hat{\mathbf{E}}_T, \hat{\mathbf{E}}_N\}$ is placed at the point $\vec{\mathbf{q}}$ and the basis vector $\hat{\mathbf{E}}_T$ is identified with $\hat{\mathbf{E}}(\vec{\mathbf{q}})$ —the tangent vector at $\vec{\mathbf{q}}$ (see Figure 6). Note that $\hat{\mathbf{E}}_T$ is drawn at an angle θ —the local orientation measured relative to the horizontal axis in retinotopic coordinates—such that $(\vec{\mathbf{q}}, \theta) \in \mathbb{R}^2 \times S^1$. Nearby tangents are displaced in both position and orientation according to the covariant derivatives of the underlying pattern. These covariant derivatives, $\nabla_{\vec{\mathbf{V}}}\hat{\mathbf{E}}_T$ and $\nabla_{\vec{\mathbf{V}}}\hat{\mathbf{E}}_N$, are naturally represented as vectors in the basis $\{\hat{\mathbf{E}}_T, \hat{\mathbf{E}}_N\}$ itself:

$$\begin{pmatrix} \nabla_{\vec{\mathbf{V}}}\hat{\mathbf{E}}_T \\ \nabla_{\vec{\mathbf{V}}}\hat{\mathbf{E}}_N \end{pmatrix} = \begin{bmatrix} w_{11}(\vec{\mathbf{V}}) & w_{12}(\vec{\mathbf{V}}) \\ w_{21}(\vec{\mathbf{V}}) & w_{22}(\vec{\mathbf{V}}) \end{bmatrix} \begin{pmatrix} \hat{\mathbf{E}}_T \\ \hat{\mathbf{E}}_N \end{pmatrix}. \quad (2.1)$$

The coefficients $w_{ij}(\vec{\mathbf{V}})$, known as *1-forms*, are functions of the displacement direction vector $\vec{\mathbf{V}}$, and since the basis $\{\hat{\mathbf{E}}_T, \hat{\mathbf{E}}_N\}$ is orthonormal, they are skew symmetric $w_{ij}(\vec{\mathbf{V}}) = -w_{ji}(\vec{\mathbf{V}})$. Thus, $w_{11}(\vec{\mathbf{V}}) = w_{22}(\vec{\mathbf{V}}) = 0$, and the system reduces to:

$$\begin{pmatrix} \nabla_{\vec{\mathbf{V}}}\hat{\mathbf{E}}_T \\ \nabla_{\vec{\mathbf{V}}}\hat{\mathbf{E}}_N \end{pmatrix} = \begin{bmatrix} 0 & w_{12}(\vec{\mathbf{V}}) \\ -w_{12}(\vec{\mathbf{V}}) & 0 \end{bmatrix} \begin{pmatrix} \hat{\mathbf{E}}_T \\ \hat{\mathbf{E}}_N \end{pmatrix}. \quad (2.2)$$

Figure 5: *Facing page*. Abstracting long-range horizontal connections as relationships between points in $\mathbb{R}^2 \times S^1$. (a) Since visual integration must involve not only the relative orientation between RFs but their spatial offset as well, it is more fully abstracted by relationships between points in $\mathbb{R}^2 \times S^1$. The exact nature of these relationships is determined by the underlying integration model. (b) Redrawing $\mathbb{R}^2 \times S^1$ fibers as orientation hypercolumns in V1 reveals the connection between the integration model in $\mathbb{R}^2 \times S^1$ and the distribution of long-range horizontal connections between the hypercolumns. (c) Collapsing the $\mathbb{R}^2 \times S^1$ abstraction to a cortical orientation map (i. e., flattening each orientation cylinder and redistributing its orientation-selective parts as orientation columns in the superficial cortical layers), the integration model implies a particular set of long-range horizontal connections between orientation domains (colors represent orientation tuning similar to panels a and b and Figure 4). Such links have been identified and measured through optical imaging and anatomical tracing (e.g., Malach et al., 1993; Bosking et al., 1997; Buzás et al., 1998) and thus can be compared to the model's predictions. (d) A real counterpart to the schematic in panel c. Reproduced from Bosking et al. (1997), this image shows an optical image of intrinsic signals combined with long-range horizontal connections traced through extracellular injection of biocytin. The white dots at the upper left corner represent the injection site, while the black dots represent labeled boutons. The white bar in the inset represents the orientation preference at the injection site.

This last system is known as Cartan's *connection equation* (O'Neill, 1966), and $w_{12}(\vec{V})$ is called the *connection form*. Since $w_{12}(\vec{V})$ is linear in \vec{V} , it can be represented in terms of $\{\hat{E}_T, \hat{E}_N\}$:

$$w_{12}(\vec{V}) = w_{12}(a \hat{E}_T + b \hat{E}_N) = a w_{12}(\hat{E}_T) + b w_{12}(\hat{E}_N) .$$

The relationship between nearby tangents is thus governed by two scalars at each point. We define them as follows,

$$\begin{aligned} \kappa_T &\triangleq w_{12}(\hat{E}_T) \\ \kappa_N &\triangleq w_{12}(\hat{E}_N), \end{aligned} \quad (2.3)$$

and interpret them as tangential (κ_T) and normal (κ_N) curvatures, since they represent a directional rate of change of orientation in the tangential and normal directions, respectively.

While the connection equation describes the local behavior of orientation for the general 2D case, it is equally useful for the 1D case of curves. Now, only $\nabla_{\hat{E}_T}$ is relevant and equation 2.2 simplifies to

$$\begin{pmatrix} \nabla_{\hat{E}_T} \hat{E}_T \\ \nabla_{\hat{E}_T} \hat{E}_N \end{pmatrix} = \begin{bmatrix} 0 & w_{12}(\hat{E}_T) \\ -w_{12}(\hat{E}_T) & 0 \end{bmatrix} \begin{pmatrix} \hat{E}_T \\ \hat{E}_N \end{pmatrix}. \quad (2.4)$$

In its more familiar form, where T, N , and κ replace \hat{E}_T, \hat{E}_N , and κ_T , respectively, this is the classical Frenet equation (O'Neill, 1966) (primes denote derivatives by arc length):

$$\begin{pmatrix} T' \\ N' \end{pmatrix} = \begin{bmatrix} 0 & \kappa \\ -\kappa & 0 \end{bmatrix} \begin{pmatrix} T \\ N \end{pmatrix}. \quad (2.5)$$

2.2 Integration Models and Projection Patterns of Horizontal Connections. The geometrical analysis discussed above and illustrated in Figure 6 shows how the relationship between nearby tangents depends on the covariant derivative: for *curves*, the connection is dictated by one curvature; for *texture flows*, or oriented 2D patterns, two curvatures are required. By estimating these quantities at a given retinal point \vec{q} , it is possible to approximate the underlying geometrical object, and thus a coherent distribution of tangents, around \vec{q} . This, in turn, can be used to model the set of horizontal connections that are required to facilitate the response of a cell if its RF is embedded in a visual context that reflects good continuation. Naturally, to describe such a local approximation and to use it for building projection patterns, the appropriate domain of integration must be determined. However, since RF measurements provide only the tangent, possibly curvature (Dobbins, Zucker, & Cynader, 1987; Versavel, Orban, & Lagae, 1990), but not whether the stimulus pattern is a curve (1D) or a texture (2D), it is necessary to consider continuations for both.

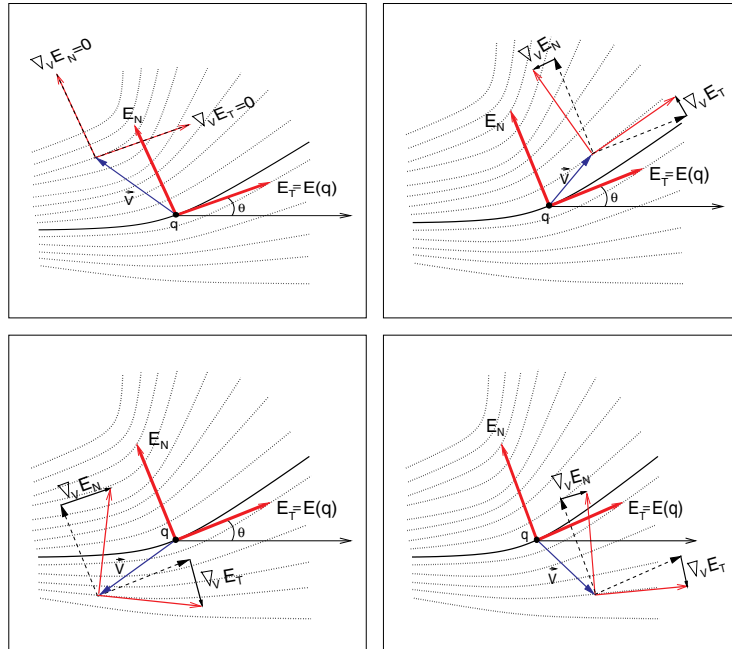
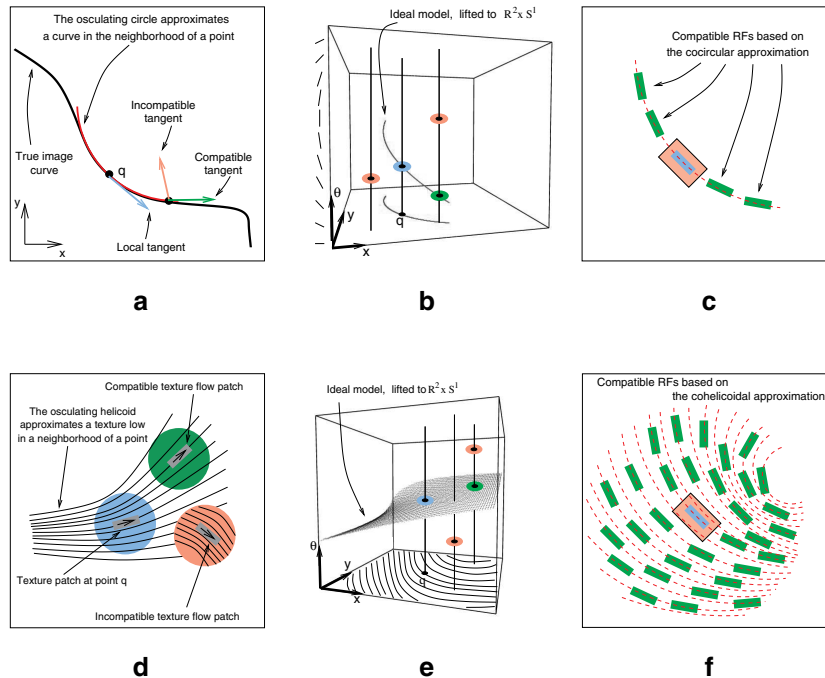


Figure 6: Visual integration under good continuation involves the question of how a measurement of orientation at one retinal position relates to another measurement of orientation at a nearby retinal position. Formally, this amounts to specifying how a tangent (orientation measurement) at position \bar{q} relates to another nearby tangent displaced by a vector \vec{V} . This tangent displacement amounts to rotation, and as shown above, this rotation can differ for different displacements. Formally, the rotation is specified locally by the covariant derivative $\Delta_{\vec{V}}$, and the mathematical analysis is facilitated by defining an appropriate coordinate frame. Shown is the Frenet basis $\{\hat{E}_T, \hat{E}_N\}$, where \hat{E}_T corresponding to a unit vector in the orientation's tangential direction and \hat{E}_N corresponds to a unit vector in the normal direction. Associated with this frame is an angle θ defined relative to external fixed coordinate frame (the black horizontal line). The covariant derivative specifies the frame's initial rate of rotation for any direction vector \vec{V} . The four different cases in this figure illustrate how this rotation depends on \vec{V} both quantitatively (i.e., different magnitudes of rotation) and qualitatively (i.e., clockwise, counterclockwise, or zero rotation). Since displacement is a 2D vector and $\Delta_{\vec{V}}$ is linear, two numbers are required to fully specify the covariant derivative. These two numbers describe the initial rate of rotation in two independent displacement directions. Using the Frenet basis once again, two natural directions emerge. A pure displacement in the tangential direction (\hat{E}_T) specifies one rotation component, and a pure displacement in the normal direction (\hat{E}_N) specifies the other component. We call them the tangential curvature (κ_T) and the normal curvature (κ_N), respectively. If visual integration based on good continuation relates to 2D patterns of orientation, then both of these curvatures are required. For good continuation along individual curves, only the tangential curvature is required since displacement is possible only in the tangential direction (that is, along the curve only).

Since estimates of curvature at point \bar{q} hold in a neighborhood containing the tangent, the discrete continuation for a curve is commonly obtained by approximating it locally by its osculating circle (do Carmo, 1976) and quantizing. This relationship, which is based on the constancy of curvature around \bar{q} , is known as *co-circularity* (Parent & Zucker, 1989; Zucker, Dobbin, & Iverson, 1989; Sigman, Cecchi, Gilbert, & Magnasco, 2001; Geisler, Perry, Super, & Gallogly, 2001), and in $\mathbb{R}^2 \times S^1$ it takes the form of a helix (see Figures 7a and 7b). Different estimates of curvature give rise to different helices whose points define both the spatial position and the local orientation of nearby RFs that are compatible with the estimate at \bar{q} (see Figure 7c). Together, these compatible cells induce a curvature-based field of long-range horizontal connections (see Figures 7a through 7c and 8a through 8d). While different curvatures induce different projection fields, the “sum” over curvatures gives an association field (see Figure 8e) reminiscent of recent psychophysical findings (Field et al., 1993). Note, however, that as a psychophysical entity, the association field is not necessarily a one-to-one reflection of connectivity patterns in the visual cortex. In fact, representing a “cognitive union” across displays of different continuations, the association field is unlikely to characterize any single cell.

Similar considerations can be applied toward the local approximation of



texture flows, although now the construction of a rigorous local model is slightly more challenging. Unlike curves, this model must depend on the estimate of *two* curvatures at the point $\bar{\mathbf{q}}$, $K_T = \kappa_T(\bar{\mathbf{q}})$ and $K_N = \kappa_N(\bar{\mathbf{q}})$, but more important, these estimates cannot be held constant in the neighborhood of $\bar{\mathbf{q}}$, however small; they must covary for the pattern to be feasible (Ben-Shahar & Zucker, 2003b). Nevertheless, invariances between the curvatures do exist, and formal considerations of good continuation have been shown to yield a unique approximation that, in $\mathbb{R}^2 \times S^1$, takes the form of a right helicoid (see Figures 7c and 7d) and whose orientation function has

Figure 7: *Facing page*. Differential geometry, integration models, and horizontal connections between RFs. (a) Estimate of tangent (light blue vector) and curvature at a point $\bar{\mathbf{q}}$ permits modeling a curve with the osculating circle as a good-continuation approximation in its neighborhood. Given the approximation, compatible (green) and incompatible (pink) tangents at nearby locations can be explicitly derived. (b) with height representing orientation (see the scale along the θ -axis), the osculating circle lifts to a helix in $\mathbb{R}^2 \times S^1$ whose points define both the spatial location and orientation of compatible nearby tangents. Color-coded as in *a*, the green point is compatible with the blue one, while the pink points are incompatible with it. (c) The consistent structure in *a* and *b* illustrated as RFs and their spatial arrangement. As an abstraction for visual integration, the ideal geometrical model—the osculating circle—induces a discrete set of RFs, which can facilitate the response of the central cell. Shown here is an example for one particular curvature tuning at the central cell. (d) For textures, determination of good continuation requires two curvatures at a point. Based on these curvatures, a local model of good continuation can determine the position, orientation, and curvatures of (spatially) nearby coherent points. Given these two curvatures at a point, there exists a unique model of good continuation that guarantees identical covariation of the curvature functions. Given the approximation, compatible (green) and incompatible (pink) flow patches at nearby locations can be explicitly derived. (e) In $\mathbb{R}^2 \times S^1$, our model for 2D orientation good continuation lifts to a right helicoid, whose points define both the spatial location and orientation of compatible (green) nearby flow tangents. (f) As an abstraction for visual integration, the ideal geometric model—the right helicoid—induces a discrete set of RFs, which can facilitate the response of the central cell. Note that broad RF tuning means that both the helix and the helicoid must be dilated appropriately, thus resulting in compatible “volumes” in $\mathbb{R}^2 \times S^1$ and possibly multiple compatible orientations at give spatial positions. This dilation should be reflected in the set of compatible RFs and the horizontal links to them, but to avoid clutter, we omit it from this figure. The effect of this dilation is illustrated in Figure 8 and consequently in all our calculations.

the following expression:

$$\theta(x, y) = \tan^{-1} \left(\frac{K_T x + K_N y}{1 + K_N x - K_T y} \right). \quad (2.6)$$

The unique property of this object is that it induces an identical covariation of the two curvature functions κ_T and κ_N in the neighborhood of the point \bar{q} . The osculating helicoid is the formal 2D analog of the osculating circle and, as with co-circularity for curves, the fields of connections between neurons that this model generates (see Figures 8f through 8j) depend intrinsically on curvature(s). Such connectivity structures can be used to compute coherent texture and shading flows in a neural, distributed fashion (Ben-Shahar & Zucker, 2003b). Two examples are shown in Figure 9.

3 Results

The computational connection fields generated above contain all the geometrical information needed for predictions about long-range horizontal connections of individual cells (or, after some averaging, that of tracer injection sites) in visual cortex. Thus, we now turn to the central question: How well do these connectivity maps match the available data about projection fields in visual cortex? In particular, do they make better predictions than those arising from collinearity or association field models?

To answer these questions, we focused on anatomical studies that report population statistics (Malach et al., 1993; Bosking et al., 1997) and compared their data to predictions produced by performing “computational anatomy” on our model.³ We randomly sampled the population of model-generated fields analogous to the way anatomists sample cells, or injection sites, in neural tissue and computed both individual and population statistics of their connection distributions. To generate robust predictions, we repeated these sampling procedures many times and calculated the expected values and standard errors of the frequency distribution.

3.1 Computational Anatomy Predicts Biological Measurements. Figure 10 illustrates the main results computed from our models, and compares them to the corresponding anatomical data reported in the literature (Malach et al., 1993; Bosking et al., 1997). The agreement of the computational process to the biological data is striking qualitatively and quantitatively. As with the association field, our model correctly predicts the spread of the pooled distribution with similar peak height (approximately

³ Anatomical studies such as Bosking et al. (1997) and Malach et al. (1993) were preferred to psychophysical or electrophysiological studies, which typically contribute no population statistics and are generally more difficult to interpret directly in terms of the structure of horizontal connections.

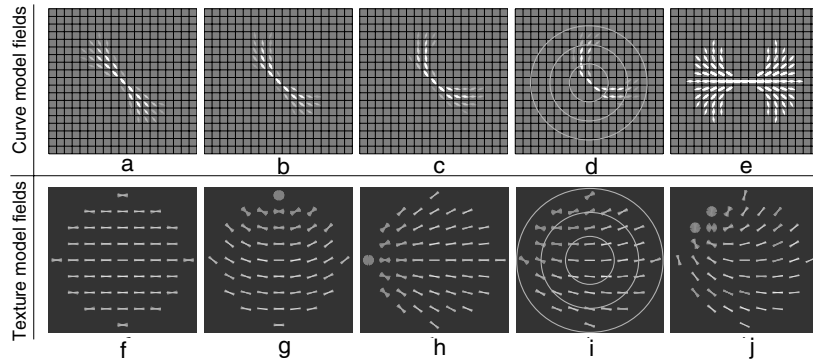


Figure 8: Illustration of connection fields for curves (top, based on co-circularity, Parent & Zucker, 1989) and textures (bottom, based on right helicoidal model, Ben-Shahar & Zucker, 2003b). Each position in these fields represents one orientation hypercolumn, while individual bars represent the orientation preference of single neurons, all of which are connected to the central cell in each field. Multiple bars at any given point represent multiple neurons in the same hypercolumn that are connected to the central cell, a result of the dilation of the compatible structure due to broad RF tuning (see the caption of Figure 7). All fields assume that orientation tuning is quantized to 10 degrees and their radius of influence is set to four to five nonoverlapping hypercolumns to reflect a 6 to 8 mm cortical range of horizontal connections (Gilbert & Wiesel, 1989) and hypercolumn diameter of 1.5 mm (to account for ocular dominance domains). (a–d) Examples of co-circularity projection fields (Parent & Zucker, 1989) for cells with orientation preference of 150 degrees (center bars) and different values of curvature tuning based on the implementation by Iverson (1994). (a) $\kappa = 0.0$ (curvature in units of pixels^{-1}). (b) $\kappa = 0.08$. (c) $\kappa = 0.16$. (d) $\kappa = 0.24$. (e) The union of all projection fields of all cells with same orientation preference (0 degrees in this case) but different curvature tuning. Note the similarity to the schematic association field in Figure 6b. (f–j) Examples of the texture flow projection fields (Ben-Shahar & Zucker, 2003b) for cells with horizontal orientation preference (center bars) and different curvature tuning. Note the intrinsic dependency on curvatures and the qualitatively different connectivity patterns that they induce. (f) $(\kappa_T, \kappa_N) = (0.0, 0.0)$. (g) $(\kappa_T, \kappa_N) = (0.2, 0.0)$. (h) $(\kappa_T, \kappa_N) = (0.0, 0.2)$. (i) $(\kappa_T, \kappa_N) = (0.1, 0.1)$. (j) $(\kappa_T, \kappa_N) = (0.2, 0.2)$. Note that while the majority of connections link cells of roughly similar orientation, some connect cells of large orientation differences. The fields shown are just a few examples sampled from the models, both of which contain similar (rotated) connection fields for each of the possible orientation preferences in the central hypercolumn. The circles superimposed on *d* and *i* are used to characterize retinotopic distance zones for the predictions made in Figure 15.

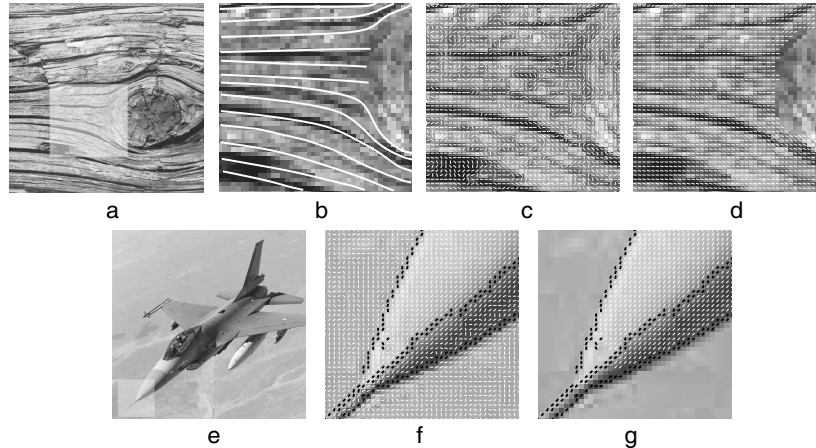


Figure 9: Example of coherent texture (a–d) and shading (e–g) flow computation based on contextual facilitation with right helicoidal connectivity patterns (Ben-Shahar & Zucker, 2003b). (a) Natural image of a tree stump with perceptual texture flow. (b) A manually drawn flow structure as perceived by a typical observer. (c) Noisy orientation field reminiscent of RF responses. The computed measurements are based on the direction of the image intensity gradient. (d) The outcome of applying a contextual and distributed computation (Ben-Shahar & Zucker, 2003b) which facilitates the response of individual cells based on their interaction with nearby cells through the connectivity structures in Figure 8. Compare to *b* and note how the measurements in the area of the knot, where no RF is embedded in a coherent context, were rejected altogether. (e) An image of a plane. (f) Measured shading field (white) and edges (black). In biological terms, edges are measured by RFs of particular orientation preferences tuned to high spatial frequencies. The shading field may be measured by cells tuned to low frequencies. (g) Applying the right helicoidal-based computation on the shading information results in a coherent shading field on the plane's nose and a complete rejection of the incoherent shading information on the textured background. Such an outcome can be used to segment smoothly curved surfaces in the scene (Ben-Shahar & Zucker, 2003b), to resolve their shape (Lehky & Sejnowski, 1988), to identify shadows (Breton & Zucker, 1996), and to determine occlusion relationship underlying edge classification (Huggins et al., 2001).

11% for orientation resolution of 10 degrees) and a similar orientation offset at which it crosses the uniform distribution (approximately ± 40 degrees). Unlike collinearity and association field models, however, ours predict qualitative differences between distributions of individual neurons, or injection sites, similar to findings in the literature (see Figure 10c). Most important, our model predicts the consistently nonmonotonic standard deviation. At orientation resolution of 10 degrees, both the anatomical data and the com-

putational models exhibit variance local minima at approximately ± 30 degrees. This property holds for both a random sample of cells (see Figure 11) and the computational population as a whole (not shown for space consideration).

3.2 Curvature Quantization and Population Statistics. The geometrical model discussed in this article must be quantized in both orientation and curvature before projection patterns can be computed and computational predictions can be made. We fixed the orientation quantization to the same level used in Bosking et al. (1997). Curvature quantization, however, is not addressed in the physiological literature, and thus it is necessary to examine its effect on the resultant connectivity distributions. We note that even with orientation represented to hyperacuity levels, there are sufficient numbers of cells to represent such quantization (Miller & Zucker, 1999).

Broad orientation tuning implies discrete orientation quantization and suggests even more discrete curvature quantization. The results presented in Figures 10 and 11 are based on quantizing curvature into five classes.⁴ This is a likely upper bound, given the broad bandpass tuning of cortical neurons that have been observed (Dobbins et al., 1987; Versavel et al., 1990) and modeled (Dobbins, Zucker, & Cynader, 1989). However, to study the effect of curvature quantization, we repeated the entire set of computations with both a smaller (three) and a larger (seven) number of curvature classes. Three is clearly the lower limit, which may correspond to the tree shrew (Bosking et al., 1997) or other simple mammals, and seven is more than required computationally (Ben-Shahar, & Zucker, 2003b). We found that all of the properties predicted initially remain invariant under these changes. In particular, regardless of quantization level, the pooled distribution remains unimodal, it peaks at zero orientation difference with approximately 11%, it crosses the uniform distribution at ± 40 degrees, and it has nonmonotonic variance with local minima at ± 30 degrees (with somewhat increased variance around zero orientation for higher quantization levels). Qualitative differences between individual neurons are predicted regardless of the number of curvature classes. All these results are illustrated in Figure 12.

3.3 Relationship Between Cells' Distribution and Connections' Distribution. Since both anatomical and computational studies must sample the population of (biological or computational) cells to measure the distribution of their horizontal connections, an important consideration is whether the underlying distribution of cells (based on their curvature tuning) can affect the pooled distribution of connections. For example, if most cells in

⁴ In the context of curves, these five classes may be labeled as straight, slowly curving to the left, slowly curving to the right, rapidly curving to the left, and rapidly curving to the right.

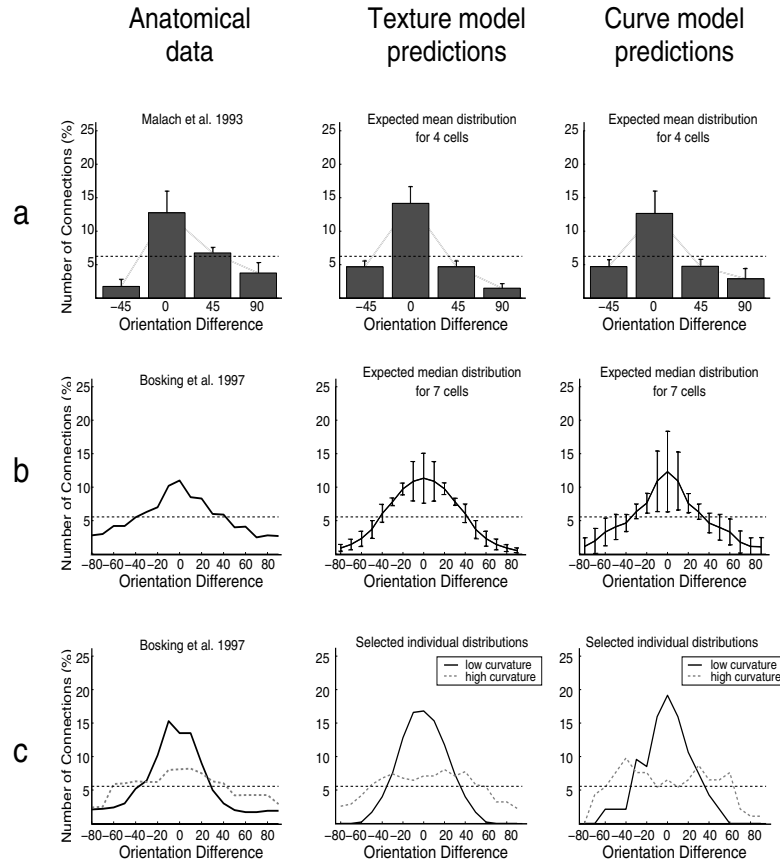


Figure 10: Comparison of anatomical data and model predictions for the distribution of long-range horizontal connections in the orientation domain. In all graphs, dashed horizontal lines represent the uniform distribution, and error bars represent ± 1 standard error. (a) Mean connection distribution of four injection sites from Malach et al. (1993) versus the computational prediction from our models (expected mean, $N = 4$, 100 repetitions). Note the dominant peak around zero orientation difference and the considerable width of the histogram. The asymmetry in the pooled distribution measured by Malach et al. (1993) likely derives from a bias at the injection site (see their Fig. 4D) rather than being intrinsic. (b) Median distribution of seven injection sites from Bosking et al. (1997) against the computational prediction from our models (expected median, $N = 7$, 100 repetitions). Note in particular the similarity in peaks' height and in the orientation offset at which the graphs cross the uniform distribution, and the strongly nonmonotonic behavior of the variance. (c) Two individual injection sites with qualitatively different connection distributions reproduced from Bosking et al. (1997). The counterpart computational instances are sampled from our models. Solid graphs correspond to the fields in Figures 8b and 8i. Dashed graphs correspond to the fields in Figures 8c and 8j.

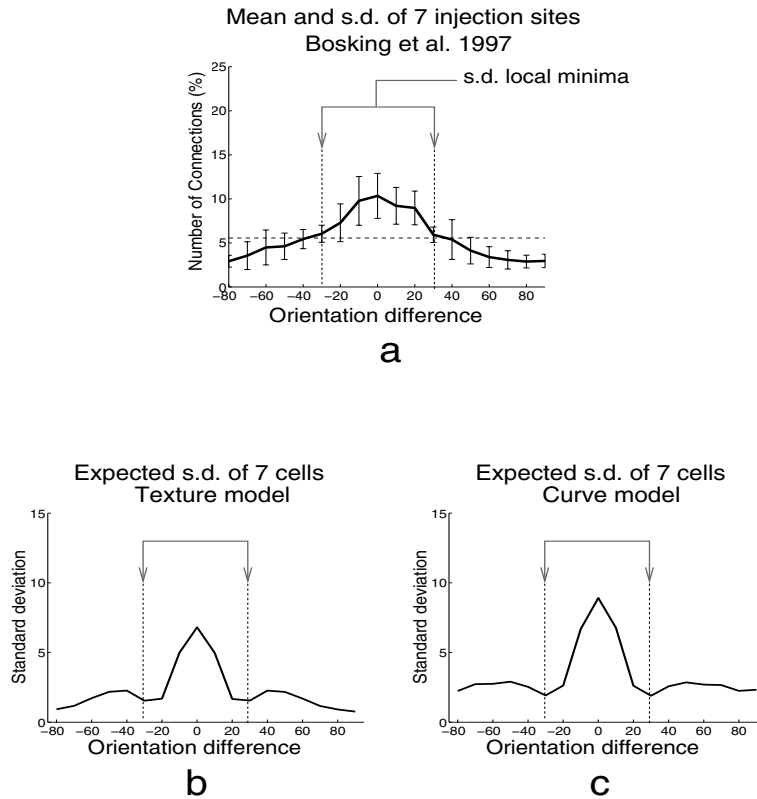


Figure 11: Although both the computational and the physiologically measured distributions of the mean are monotonically decreasing, their standard deviation is consistently nonmonotonic. (a) While Bosking et al. (1997) used the population median, we further analyzed their published data (from seven injection sites) to find its mean and standard deviation. It is evident that the standard deviation is nonmonotonic, with two local minima at ± 30 degrees (marked with arrows). (b) Expected standard deviation for the texture model. (c) Expected standard deviation for the curve model. Both graphs depict the expected standard deviation for seven randomly selected cells ($N = 7$, 100 repetitions), and both show a similar nonmonotonic behavior with pronounced standard deviation local minima at approximately ± 30 degrees. Note how the computational local minima coincide with the anatomical ones (arrows are copied from *a* and overlaid on the computational graphs). Compare also to the standard deviation on the median graphs in Figure 10b. Note that as with the distributions themselves, both computational models produce quantitatively similar standard deviation results.

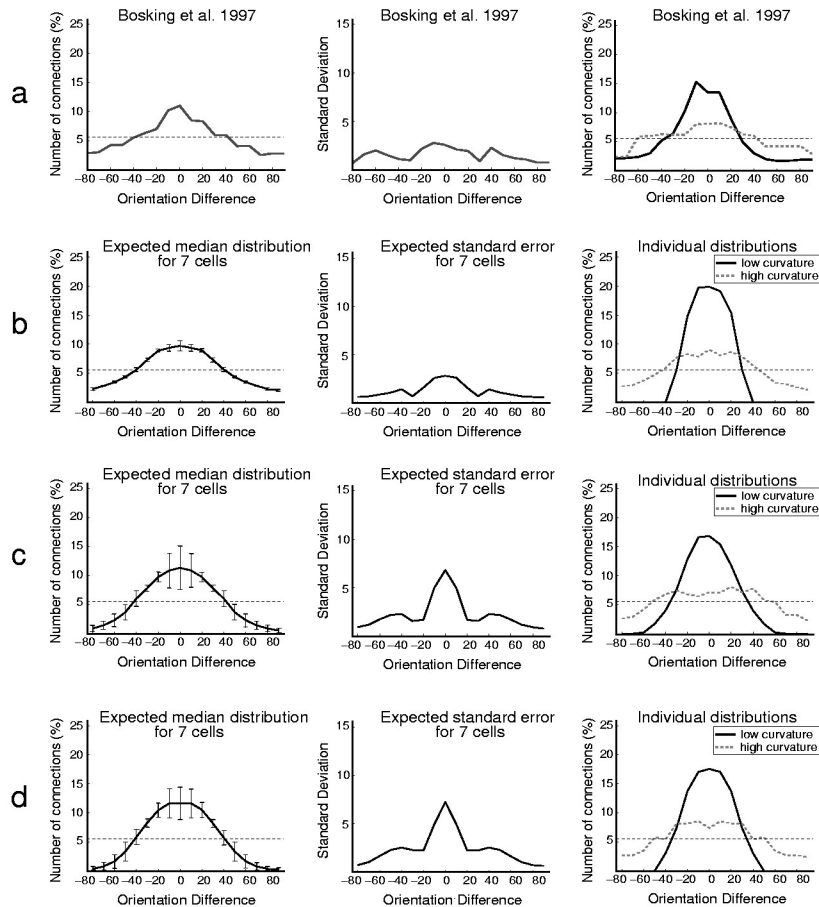


Figure 12: Different quantization levels of curvature tuning have little effect on the expected median distribution and its standard deviation. (a) Anatomical data from Bosking et al. (1997) shown for comparison with the computational predictions. (b) Computational predictions with three curvature classes. (c) Computational predictions with five curvature classes. (d) Computational predictions with seven curvature classes. In all cases, the left column depicts the expected median for seven cells (bars are 1 s.d.), the middle column depicts the expected standard deviation for seven cells, and the right column shows two qualitatively different distributions from two different cells. For space considerations, we show the results from the texture model only.

the population are tuned for zero or very small curvature, the pooled connection distribution may differ from that of a population dominated by high curvature cells.

The results presented in Figures 10 and 11 are based on the assumption that cells of different curvature tuning (or, put differently, of different connectivity patterns) are distributed uniformly. Such an assumption follows naturally from the mathematical abstraction that allocates the same number of computational units to equal portions of $\mathbb{R}^2 \times S^1$. However, if this assumption were wrong, would a bias in the distribution of cells affect significantly the predictions made from our models?

Unfortunately, few data about such distributions are available, partially because anatomists need not assume any particular cells' distribution for their measurements of projection fields, and partially because curvature tuning is rarely considered. Some data available on the distribution of end-stopped cells (Kato, Bishop, & Orban, 1978; Orban, 1984) in conjunction with the functional equivalence of end stopping with curvature selectivity (Orban, Versavel, & Lagae 1987; Dobbins et al., 1987, 1989; Versavel et al., 1990), suggest that cells are distributed *bimodally* in the curvature domain, with peaks at both zero and high curvature tuning. Alternatively, statistical studies of edge correlations in natural images (Dimitriv & Cowan, 1998; August & Zucker, 2000; Sigman et al., 2001; Kaschube, Wolf, Geisel, & Löwel, 2001; Geisler et al., 2001; Pedersen & Lee, 2002) show that collinear co-occurrences are more frequent than others. Although these co-occurrence measurements neither depend on curvature nor do they necessarily indicate any particular distribution of cells at the computational level, implicitly they may suggest that cells are distributed *unimodally* in the curvature domain, with peak at zero curvature only.

Since our model raises the possibility of a curvature bias effect, we thus redistributed the population of our computational cells by one or the other of these nonuniform (bimodal and unimodal) distributions, and then repeated the computational anatomy process described in section 3.1. All computations were done on the more general 2D (texture) model. The bimodal distribution was modeled as a radial two-gaussian mixture model (GMM) parameterized by the total curvature $\kappa = \sqrt{\kappa_T^2 + \kappa_N^2}$ and parameters $\mu_0 = 0$, σ_0 , μ_1 , and σ_1 . The unimodal distribution was modeled as a 2D gaussian of zero mean and variances σ_T and σ_N in the κ_T and κ_N dimensions, respectively.

Figure 13 illustrates one example of the resultant statistical measures for the bimodal cell distribution. In this example, $\sigma_0 = 0.04$ and $\sigma_1 = 0.05$, where the slight difference accounts for corresponding differences in the two modes as reported in Kato et al. (1978) and Orban (1984). As is shown, this nonuniform distribution hardly changes the expected median, while further emphasizing the nonmonotonic nature of the variance (compared to the statistics obtained with the same number of curvature classes and

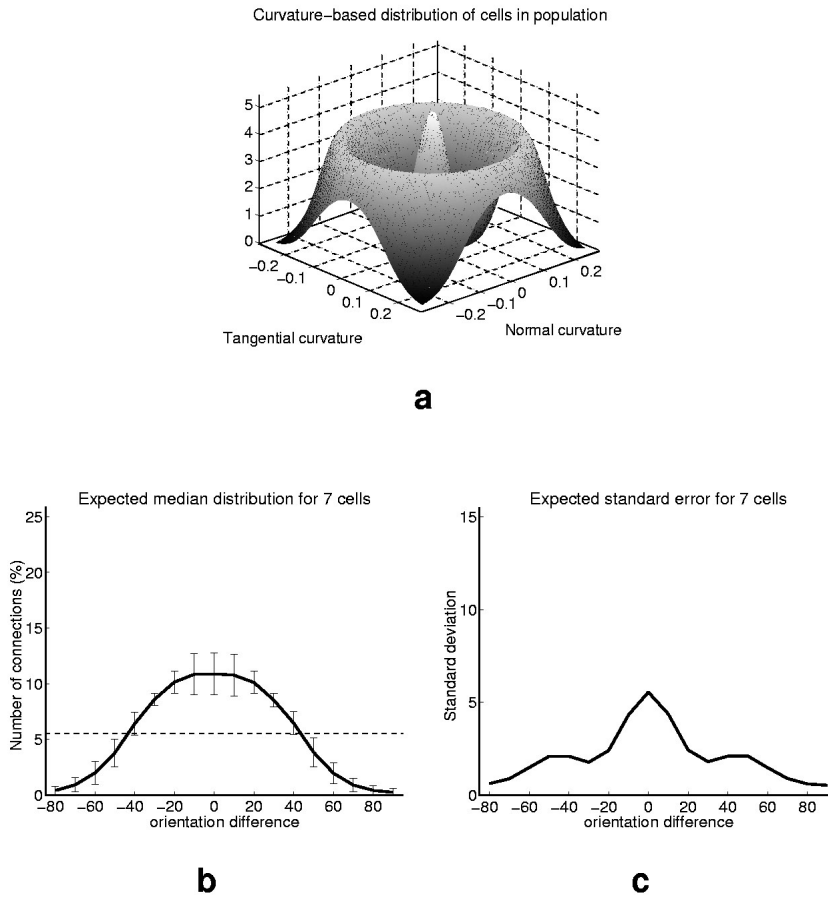


Figure 13: A statistical confirmation that the properties of our models persist even when the population of cells is distributed bimodally (Kato et al., 1978; Orban, 1984). Illustrated here is the result from a distribution modeled as a GMM with $\mu_0 = 0$, $\sigma_0 = 0.04$, $\mu_1 = 0.2$, and $\sigma_1 = 0.05$. Since the bimodal nature of the distribution is best represented with a higher number of curvature classes, presented here is the case of the texture model with curvatures quantized to seven classes each. (a) The (radially) bimodal distribution of cells in the curvature domain normalized for number of cells. The x - and y -axes represent tangential and normal curvature tuning, respectively, and the z -axis represents the number of such curvature-tuned cells for any given orientation tuning. (b) Expected median of seven cells. Error bars are ± 1 standard deviation. (c) Expected standard error for seven cells. Compare both graphs to Figure 12d.

uniform cell distribution; see Figure 12d). Similar results were obtained with other values of σ_0 and σ_1 and for the curvature quantized to five classes as well.⁵

Figure 14 illustrates another example, this time using the unimodal cell distribution mentioned above. In this example, $\sigma_T = \sigma_N = 0.15$ such that cells with zero curvature tuning are eight times more frequent than cells tuned to the maximum value of curvatures. As expected, this strongly nonuniform distribution slightly elevated the peak of the population statistics, but otherwise, all other features that were predicted from the uniform cell distribution, and in particular the nonmonotonic variance, were fully preserved. Similar results were obtained with other values of σ_T and σ_N , and for all quantization levels of the curvatures (as in section 3.2).

In summary, we have shown that even if cells in primary visual cortex were distributed nonuniformly in their curvature tuning, the pooled distribution of long-range horizontal connections in the orientation domain would preserve its fundamental properties, and in particular its wide spread and nonmonotonic variance. Thus, our conclusions are not biased by an implicit assumption about curvature-dependent distribution of cells.

4 Discussion

The findings presented from our computational anatomy support the functional identification of the long-range horizontal connections with those obtained mathematically. However, the question of why the texture model is necessary becomes unavoidable, and we believe this issue is more than just formal mathematics. Certain physiological and psychophysical findings, such as iso-orientation side facilitation (Adini et al., 1997), functional and anatomical connections between retinotopically *parallel* receptive fields (Ts'o et al., 1986; Gilbert & Wiesel, 1989), and roughly isotropic retinotopic extent of projection fields (Malach et al., 1993; Sincich & Blasdel, 2001) suggest the perceptual integration of texture flows rather than curves. Although this class of patterns may seem less important than curves as a factor in perceptual organization, their perceptual significance has been established (Glass, 1969; Kanizsa, 1979; Todd & Reichel, 1990). Furthermore, recent computational vision research implicates them in the analysis of visual shading (Lehky & Sejnowski, 1988; Huggins, Chen, Belhumeur, & Zucker, 2001), as was demonstrated in Figure 9, and even color (Ben-Shahar & Zucker, 2003a).

Whether projection patterns of cells in primary visual cortex come in different flavors (i.e., curve versus texture or shading integration) is an open question. To answer it, one is likely to exploit the many physiologically measurable differences between these classes of projection patterns, as sug-

⁵ Quantization of curvature to three classes was irrelevant in this case because the bimodality of the distribution could not be expressed using too few (three) samples.

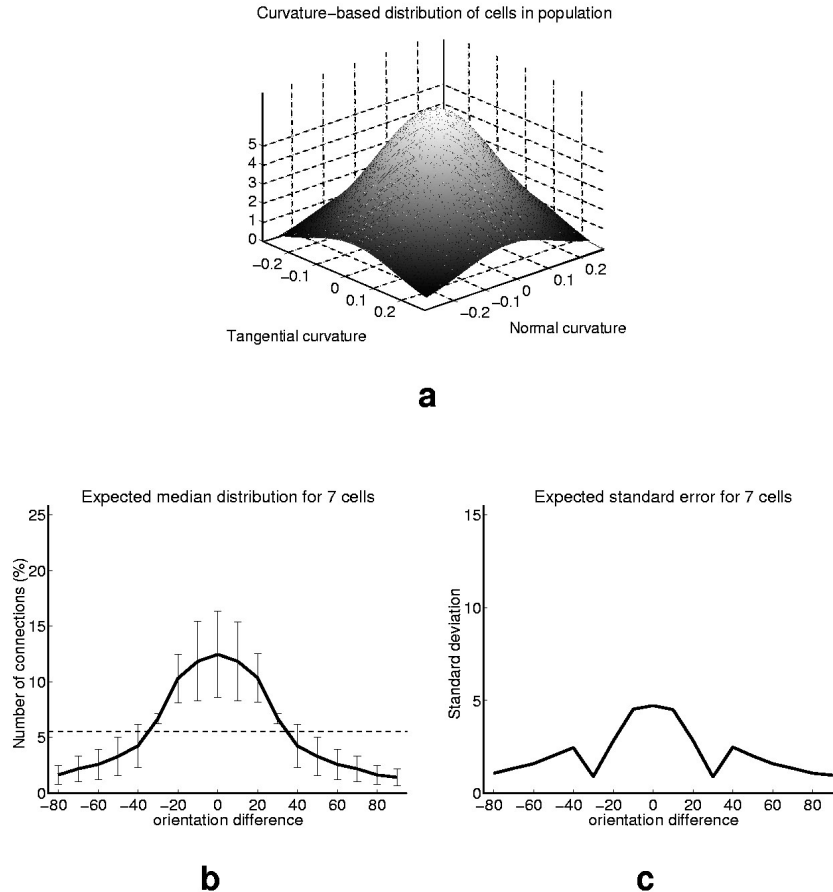


Figure 14: A statistical confirmation that the properties of our models persist even when the population of cells is distributed normally (i.e., *unimodally*). Such distribution is implicitly suggested by statistics of edges in natural images (Dimitriv & Cowan, 1998; August & Zucker, 2000; Sigman et al., 2001; Kaschube et al., 2001; Geisler et al., 2001; Pedersen & Lee, 2002) in which collinear edges are much more frequent. The case presented here ($\sigma_T = \sigma_N = 0.15$) induces a distribution in which cells of zero curvature tuning are eight times more frequent than those of maximal curvature tuning. The graphs in this figure correspond to the texture model with curvatures quantized to three classes each. Similar results were obtained with other quantization levels as well. (a) The normal distribution of cells in the curvature domain normalized for number of cells. The x - and y -axes represent tangential and normal curvature tuning, respectively, and the z -axis represents the number of such curvature-tuned cells for any given orientation tuning. (b) Expected median of seven cells. Error bars are ± 1 standard deviation. (c) Expected standard error for seven cells. Compare both graphs to Figure 12b.

gested by Figure 8. Unfortunately, the statistical data obtained so far do not distinguish between the two (curve and texture) integration models; without a spatial dimension, the statistical differences between the two models in the orientation domain are too fine to measure relative to the accuracy of current laboratory techniques.

Until full spatio-angular data are obtained, however, the inclusion of even weak spatial information is sufficient to generate further testable predictions. In particular, incorporating the retinotopic distance between linked cells into the statistics (or estimating it from their cortical distance) can produce predictions regarding the dependency of the distribution's spread and shape on the integration distance, as illustrated in Figure 15. Some verification for these predictions can be seen in the measurements of Kisvárdy et al. 1997, top row in their Fig. 9 shows developing peaks resembling the ones in Figures 15b, and 15c). Similar annular analyses, which focus on sectors of the annuli in directions other than parallel to the RF's preferred orientation, provide measurable differences between curve and texture projection fields.

In summary, we have presented mathematical analysis and computational models that predict both the pooled distribution of long-range horizontal connections and the distributions of individual cells and injection sites. For the first time, the modeling goes beyond the unimodal first-order data and falsifies a common conclusion from it. In particular, while co-aligned facilitation entails the pooled first-order data, the converse is not necessarily true: these data are also consistent with curvature-dependent connections. The second-order (variance) data, however, remain consistent with curvature-dependent connections but not with coaligned facilitation.

The explanatory force of our model derives from sensory integration, and we observed in Section 1 that most researchers limit this to curve integration via collinearity. We conclude in an enlarged context: differential geometry provides a foundation for connections in visual cortex that predicts both dependency on curvature(s) and an expanded functional capability, including curve, texture, and shading integration. Since the same geometrical analysis applies to many other domains in which orientation and direction fields are fundamental features, coherent motion processing (Series, Georges, Lorenceau, & Frégnac, 2002) and coherent color perception (Ben-Shahar & Zucker, 2003a) might also have been included. Since all follow from the geometry and all are important for vision, more targeted experiments are required to articulate their neural realization.

Appendix: Noise Models

Two basic noise models are used in this article to examine whether variations of the basic collinear distribution (see Figure 2) can produce a pooled statistics with similar properties to the biological one. This appendix describes both procedures in detail.

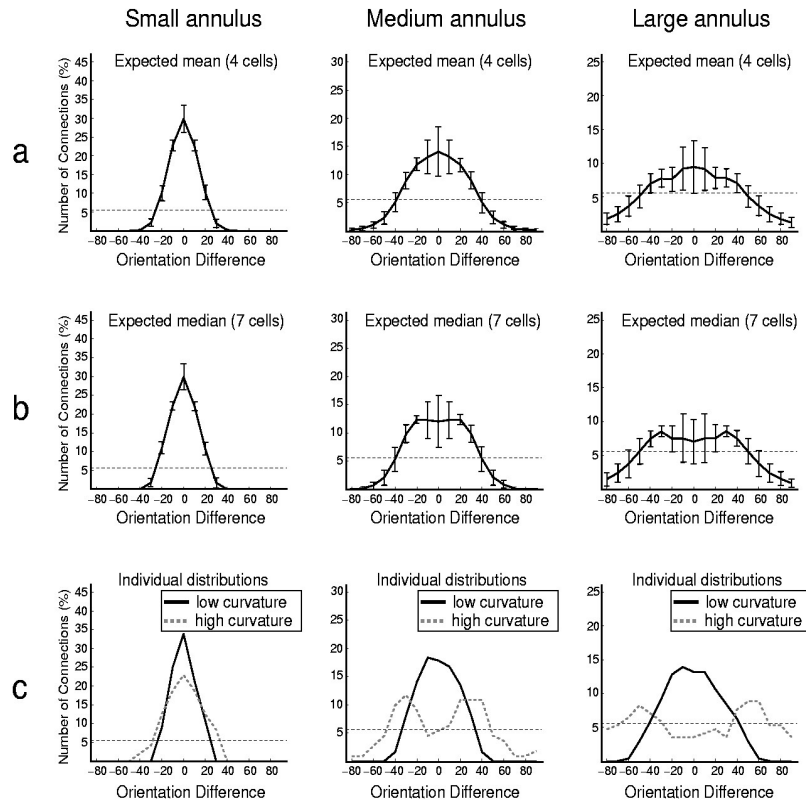


Figure 15: Model predictions of connection distributions by a retinotopic annulus. Left, middle, and right columns correspond to predictions based on small, medium, and large annuli, respectively (circles in Figures 8d and 8i). All annuli refer to distances beyond one orientation hypercolumn, thus, the small annulus should not be confused with distances less than the diameter of one hypercolumn. In *a* and *b* the same sampling procedure and the same sample set sizes described in Figure 10 were repeated. For lack of space, we omit the very similar graphs of the mean and median of the entire population, and present predictions from the texture model only. (a) Expected mean distribution and standard error ($N = 4, 100$ repetitions). Note the spread with increased retinotopic distance. (b) Expected median distribution and standard error ($N = 7, 100$ repetitions). Note the developing symmetric peaks that further depart from the iso-orientation domain as the spatial distance increases. The correspondence of these peaks to the minima of the standard error is remarkable, thus designating them as statistical anchors suitable for empirical verification. (c) Individually tuned cells show the qualitative difference between distributions of high and low curvature cells. In particular, note how the distributions of medium and high curvature cells (dashed graphs) are the ones that develop the peaks mentioned in *b* above.

To examine natural random variations at the level of individual connections, each long-range horizontal connection, ideally designated to connect cells of orientation difference $\Delta\theta$, is shifted to connect cells of orientation difference $\Delta\theta + \epsilon_\sigma$, where ϵ_σ is a wrapped gaussian noise with zero mean and variance σ . To do this computation, the base distribution (collinear or association field) from Figure 2, initially given as probabilities over 18 orientation bins of 10 degrees each, was normalized and quantized to a connection histogram in the range $[0, N]$, where N represents the total number of connections a cell makes. To each such connection to orientation difference $\Delta\theta$ we then added a wrapped gaussian noise ϵ_σ of zero mean and variance σ , and the new (random) connection was accumulated at the bin $\Delta\theta + \epsilon_\sigma$ of the resultant histogram. This process was repeated 200 times to produce 200 different perturbations, from which both expected distribution and variance were computed bin-wise. The parameter σ was set to the value that produced an expected distribution of peak height and spread similar to the biological one. Since different anatomical studies and protocols indicate a different number of total connections (e.g., hundreds in Schmidt et al. 1997, approximately 3500 in Buzás et al., 1998 and up to 20,000 for injection sites of approximately 20 cells in Bosking et al., 1997), we repeated this statistical test for normalizations in different ranges. As expected, changing N only scaled the variance uniformly across the expected distribution but did not affect its mean. Thus, for better clarity of its monotonicity, the result in Figure 3b reflects a smaller number of total connections ($N = 200$), as in, for example, Schmidt et al. (1997).

To examine random variations due to “leakage” of tracer from an injection site of preferred orientation θ_0 to nearby orientation columns, we modeled such leakage by selecting $i = 1, \dots, M$ cells of preferred orientation $\theta_i = \theta_0 + \Delta\theta_\sigma$, where $\Delta\theta_\sigma$ is a wrapped gaussian random variable of zero mean and variance σ . A normalized- and quantized-based distribution (collinear or association field) was then centered around each of θ_i , and all were summed up and normalized to yield a resultant (random) distribution of connections for the injection site at θ_0 . As before, we repeated this generation process 200 times to produce 200 different perturbations, from which both expected distribution and variance were computed bin-wise. The parameter σ was again set to that value that produced an expected distribution of peak height and spread similar to the biological one. The number of cells in an injection was set to $M = 20$, approximately as reported in Bosking et al. (1997) Unlike random variations at the level of individual connections, the range parameter N had no effect on the variance of the expected distribution.

Acknowledgments

We are grateful to Allan Dobbins, David Fitzpatrick, Kathleen Rockland, Terry Sejnowski, and Michael Stryker for reviewing this manuscript and for

providing valuable comments; to Lee Iverson for the curve compatibility fields in Figure 8; and to an anonymous reviewer for pointing out a possible artifact in the data (in Section 1.1). This research was supported by AFOSR, ONR, and DARPA.

References

- Adini, Y., Sagi, D., & Tsodyks, M. (1997). Excitatory-inhibitory network in the visual cortex: Psychophysical evidence. *Proc. Natl. Acad. Sci. U.S.A.*, *94*, 10426–10431.
- August, J., & Zucker, S. (2000). The curve indicator random field: Curve organization via edge correlation. In K. Boyer & S. Sarkar, (Eds.), *Perceptual organization for artificial vision systems*. Norwell, MA: Kluwer.
- Ben-Shahar, O., & Zucker, S. (2003a). Hue fields and color curvatures: A perceptual organization approach to color image denoising. In *Proc. Computer Vision and Pattern Recognition* (pp. 713–720). Los Alamitos, CA: IEEE Computer Society.
- Ben-Shahar, O., & Zucker, S. (2003b). The perceptual organization of texture flows: A contextual inference approach. *IEEE Trans. Pattern Anal. Machine Intell.*, *25*(4), 401–417.
- Bosking, W., Zhang, Y., Schofield, B., and Fitzpatrick, D. (1997). Orientation selectivity and the arrangement of horizontal connections in the tree shrew striate cortex. *J. Neurosci.*, *17*(6), 2112–2127.
- Breton, P. & Zucker, S. (1996). Shadows and shading flow fields. In *Proc. Computer Vision and Pattern Recognition* (pp. 782–789). Los Alamitos, CA: IEEE Computer Society.
- Buzás, P., Eysel, U., & Kisvárdy, Z. (1998). Functional topography of single cortical cells: An intracellular approach combined with optical imaging. *Brain Res. Prot.*, *3*, 199–208.
- Dimitriv, A. & Cowan, J. (1998). Spatial decorrelation in orientation-selective cortical cells. *Neural Comput.*, *10*, 1779–1795.
- do Carmo, M. (1976). *Differential geometry of curves and surfaces*. Engelwood Cliffs, NJ: Prentice-Hall.
- Dobbins, A., Zucker, S., & Cynader, M. (1987). Endstopped neurons in the visual cortex as a substrate for calculating curvature. *Nature*, *329*(6138), 438–441.
- Dobbins, A., Zucker, S., & Cynader, M. (1989). Endstopping and curvature. *Vision Res.*, *29*(10), 1371–1387.
- Field, D., Hayes, A., & Hess, R. (1993). Contour integration by the human visual system: Evidence for a local “association field.” *Vision Res.*, *33*(2), 173–193.
- Geisler, W., Perry, J., Super, B., & Gallogly, D. (2001). Edge co-occurrence in natural images predicts contour grouping performance. *Vision Res.*, *41*(6), 711–724.
- Gilbert, C., & Wiesel, T. (1989). Columnar specificity of intrinsic horizontal and corticocortical connections in cat visual cortex. *J. Neurosci.*, *9*(7), 2432–2442.
- Glass, L. (1969). Moiré effect from random dots. *Nature*, *223*(5206), 578–580.

- Hubel, D., & Wiesel, T. (1977). Functional architecture of macaque monkey visual cortex. *Proc. R. Soc. London Ser. B*, 198, 1–59.
- Huggins, P., Chen, H., Belhumeur, P., & Zucker, S. (2001). Finding folds: On the appearance and identification of occlusion. In *Proc. Computer Vision and Pattern Recognition*, (pp. 718–725). Los Alamitos, CA: IEEE Computer Society.
- Iverson, L.A. (1994). *Toward discrete geometric models for early vision*. Unpublished doctoral dissertations, McGill University.
- Kanizsa, G. (1979). *Organization in vision: Essays on gestalt perception*. New York: Praeger.
- Kapadia, M., Ito, M., Gilbert, C., & Westheimer, G. (1995). Improvement in visual sensitivity by changes in local context: Parallel studies in human observers and in V1 of alert monkeys. *Neuron*, 15, 843–856.
- Kapadia, M., Westheimer, G., & Gilbert, C. (2000). Spatial distribution of contextual interactions in primary visual cortex and in visual perception. *J. Neurophysiol.*, 84, 2048–2062.
- Kaschube, M., Wolf, F., Geisel, T., & Löwel, S. (2001). The prevalence of colinear contours in the real world. *Neurocomputing*, 38–40, 1335–1339.
- Kato, H., Bishop, P., & Orban, G. (1978). Hypercomplex and the simple/complex cell classification in cat striate cortex. *J. Neurophysiol.*, 41, 1071–1095.
- Kisvárdy, Z., Kim, D., Eysel, U., & Bonhoeffer, T. (1994). Relationship between lateral inhibition connections and the topography of the orientation map in cat visual cortex. *J. Neurosci.*, 6, 1619–1632.
- Kisvárdy, Z., Tóth, É., Rausch, M., & Eysel, U. (1997). Orientation-specific relationship between populations of excitatory and inhibitory lateral connections in the visual cortex of the cat. *Cereb. Cortex*, 7, 605–618.
- Lehky, S. & Sejnowski, T. (1988). Network model of shape-from-shading: Neural function arises from both receptive and projective fields. *Nature*, 333, 452–454.
- Malach, R., Amir, Y., Harel, M., & Grinvald, A. (1993). Relationship between intrinsic connections and functional architecture revealed by optical imaging and in vivo targeted biocytin injections in primate striate cortex. *Proc. Natl. Acad. Sci. U.S.A.*, 90, 10469–10473.
- Matsubara, J., Cynader, M., Swindale, N., & Stryker, M. (1985). Intrinsic projections within visual cortex: Evidence for orientation specific local connections. *Proc. Natl. Acad. Sci. U.S.A.*, 82, 935–939.
- Miller, D., & Zucker, S. (1999). Computing with self-excitatory cliques: A model and application to hyperacuity-scale computation in visual cortex. *Neural Comput.*, 11, 21–66.
- Mitchison, G., & Crick, F. (1982). Long axons within the striate cortex: Their distribution, orientation, and patterns of connections. *Proc. Natl. Acad. Sci. U.S.A.*, 79, 3661–3665.
- O’Neill, B. (1966). *Elementary differential geometry*. Orlando, FL: Academic Press.
- Orban, G. (1984). *Neural operations in the visual cortex*. Berlin: Springer-Verlag.
- Orban, G., Versavel, M., & Lagae, L. (1987). How do striate neurons represent curved stimuli. *Abstracts of the Society for Neuroscience*, 13, 404.10.
- Parent, P., & Zucker, S. (1989). Trace inference, curvature consistency, and curve detection. *IEEE Trans. Pattern Anal. Machine Intell.*, 11(8), 823–839.

- Pedersen, K., & Lee, A. (2002). *Toward a full probability model of edges in natural images* (APPTS Tech. Rep. 02-1.) Providence, RI: Division of Applied Mathematics, Brown University.
- Polat, U., & Sagi, D. (1993). Lateral interactions between spatial channels: Suppression and facilitation revealed by lateral masking experiments. *Vision Res.*, *33*(7), 993–999.
- Rockland, K., & Lund, J. (1982). Widespread periodic intrinsic connections in the tree shrew visual cortex. *Science*, *215*(19), 1532–1534.
- Schmidt, K., Goebel, R., Löwel, S., & Singer, W. (1997). The perceptual grouping criterion of colinearity is reflected by anisotropies in the primary visual cortex. *Eur. J. Neurosci.*, *9*, 1083–1089.
- Schmidt, K., & Löwel, S. (2002). Long-range intrinsic connections in cat primary visual cortex. In B. Payne & A. Peters, (Eds.), *The cat primary visual cortex* (pp. 387–426). Orlando, FL: Academic Press.
- Series, P., Georges, S., Lorenceau, J., & Frégnac, Y. (2002). Orientation dependent modulation of apparent speed: A model based on the dynamics of feed-forwards and horizontal connectivity in V1 cortex. *Vision Res.*, *42*, 2781–2797.
- Sigman, M., Cecchi, G., Gilbert, C., & Magnasco, M. (2001). On a common circle: Natural scenes and gestalt rules. *Proc. Natl. Acad. Sci. U.S.A.*, *98*(4), 1935–1940.
- Sincich, L., & Blasdel, G. (2001). Oriented axon projections in primary visual cortex of the monkey. *J. Neurosci.*, *21*(12), 4416–4426.
- Todd, J., & Reichel, F. (1990). Visual perception of smoothly curved surfaces from double-projected contour patterns. *J. Exp. Psych.: Human Perception and Performance*, *16*(3), 665–674.
- Ts'o, D., Gilbert, C., & Wiesel, T. (1986). Relationships between horizontal interactions and functional architecture in cat striate cortex as revealed by cross-correlation analysis. *J. Neurosci.*, *6*(4), 1160–1170.
- Versavel, M., Orban, G., & Lagae, L. (1990). Responses of visual cortical neurons to curved stimuli and chevrons. *Vision Res.*, *30*(2), 235–248.
- Weliky, M., Kandler, K., Fitzpatrick, D., & Katz, L. (1995). Patterns of excitation and inhibition evoked by horizontal connections in visual cortex share a common relationship to oriented columns. *Neuron*, *15*, 541–552.
- Wertheimer, M. (1955). Laws of organization in perceptual forms. In W. Ellis, (Ed.), *A source book of gestalt psychology*, (pp. 71–88). London: Routledge & Kegan Paul.
- Zucker, S., Dobbins, A., & Iverson, L. (1989). Two stages of curve detection suggest two styles of visual computation. *Neural Comput.*, *1*, 68–81.